Quantification of cancellous bone structure using symbolic dynamics and measures of complexity

Peter I. Saparin,[1,*] Wolfgang Gowin,[2] Jürgen Kurths,[1] and Dieter Felsenberg[2]
[1]*Department of Nonlinear Dynamics, Institute of Physics, Potsdam University, Am Neuen Palais 10, P.O. Box 601553, D-14415 Potsdam, Germany*
[2]*Osteoporosis Research Group, Department of Radiology and Nuclear Medicine, University Hospital B. Franklin, Free University, Hindenburgdamm 30, D-12200 Berlin, Germany*
(Received 14 April 1998; revised manuscript received 2 July 1998)

In this study we generalize symbolic dynamics to analyze two-dimensional objects and utilize measures of complexity to quantify the structure of symbol-encoded images. This technique is applied to study quantitatively the structure of human cancellous bone by analyzing computed tomography images. First, the preprocessed images are transformed into symbols, applying a mixture of static and dynamic encoding. Next, the spatial distribution of cancellous bone is evaluated using measures of complexity. New parameters are introduced to quantify the cancellous bone architecture as a whole. The results exhibit that the complexity of the structure declines more rapidly than density during the loss of bone in osteoporosis, strongly suggesting an exponential relationship between bone mass and architecture. It is found that normal bone has complex ordered structure, while the structure during the initial stage of bone loss is characterized by lower complexity and a significantly higher level of disorder, which is maximal there. A strong grade of the bone loss leads again to ordered structure, however its complexity is minimal. In addition, this method is significantly sensitive to changes in structure of natural composite materials. [S1063-651X(98)08911-9]

PACS number(s): 87.59.Fm, 05.45.+b, 07.05.Pj, 87.59.Ls

I. INTRODUCTION

During the past decade the concepts of symbolic dynamics [1,2] and measures of complexity [3–7] have been successfully utilized to analyze models and experimental data from different areas of science such as astrophysics [8], geophysics [9], stochastic systems [10], and medicine [11]. Originally, symbolic dynamics was developed to work with multivariate but one-dimensional time series. The dramatically increased quality of imaging and the number of imaging applications in different fields of science require a tool for the analysis and quantification of planar [two-dimensional (2D)] and spatial (3D) architecture, its spatial dynamics, and complexity.

In the present paper we generalize the notion of symbolic dynamics [1,5,2,12] in order to analyze two-dimensional images, develop a two-dimensional procedure of transformation into symbols, and utilize measures of complexity [11,13,14,5] to assess the composition of symbols within these images. The proposed technique is applied to quantify the architecture and structural properties of biological composite materials.

Since in any object mass and structure depend on each other to build a functional form [15], methodologies to measure structural information are needed to understand the contribution of structure to support the form and to quantify the spatial architecture, its changes, and the loss of object integrity. Bone tissue is a paradigmatic example of a highly complex structural entity [15]. Bone integrity is maintained by intertwined attributes such as strength, mass, and structure [16,17]. These intrinsic factors define the fracture risk of human bones in metabolic bone diseases. Loss of the bone leads to osteopenia (weak grade) and osteoporosis (strong grade of the disease). Osteoporosis is defined as a disease characterized by low bone mass and microarchitectural deterioration of bone tissue, leading to an increase of fracture risk [18]. Osteopenia is world-wide the most often found bone disease and is prevalent in about 54% of postmenopausal white women in the United States [19]. According to the World Health Organization definition, 16% of all white women in the U.S. age 50 years or above suffer from fractures caused by osteoporosis [19]. The estimated cost of osteoporotic fractures was 13.8 billion dollars in 1995 [20]. The financial and health-related costs of osteoporosis can only rise in future generations in every geographic region. This gives the reason for the assumption that osteoporosis will truly become a global problem over the next half-century [21] and that measures are urgently required to avert this trend.

Osteoporosis is diagnosed by medical physical examination, x-ray evaluation of the spine and other bones, and the measurement of bone mineral density. Bone mineral density (BMD) measurements [22,23] are used to measure bone mass noninvasively and serve as a surrogate to estimate bone fracture risk [23]. Note, however, the knowledge of a low bone density offers no information about the structure remaining within the volume of the bone. Bone volume is determined by soft tissue marrow occupying the space between hard bone structural elements (trabeculae), which define the composition of bone architecture. This means the knowledge of the distribution of mass within the volume is imperative to assess bone integrity and fracture risk [24,25]. Density measurements provide only information about the amount of material, omitting its architecture. Present approaches to assess bone structure are either invasive and evaluate only partial aspects of the bone structure [26–28], or, when noninvasive, apply techniques such as fractal [29], texture [30], and pat-

*Electronic address: petr@agnld.uni-potsdam.de

tern analysis [31,32] resulting in discriminatory measurements with low sensitivity [32], or only profiles of bone sections [31], or assess only projected surface patterns [29,30].

We are applying symbolic dynamics and measures of complexity as a new noninvasive approach to assess cancellous bone structure in its complex spatial distribution for the quantification of the architecture as a whole. Techniques of 2D symbolic dynamics and measures of complexity are employed to identify structural changes in human cancellous bone of vertebral bodies from preprocessed images obtained by computed tomography (CT) which are, crucially important, symbol-encoded by both static and dynamical approaches.

The results lead to new insights into bone's internal structure and provide improvements in differentiation of structural loss. We have found that normal bone has a complex ordered structure, while the structure during the initial stage of bone loss is characterized by lower complexity and a significantly higher level of disorder. Strong grade of the bone loss leads again to ordered structure, however its complexity is minimal. The complexity of the structure declines more rapidly than density during the loss of bone leading to osteoporosis, strongly suggesting an exponential relationship between bone mass and architecture.

The data are described in Sec. II. Section III presents the preprocessing algorithms we developed to segment the vertebral body from the connective and soft tissue background present in a CT image, and to split the entire vertebra into the cancellous bone and the cortical shell. Our generalization of symbolic dynamics to work with 2D images, the encoding procedure, and the set of measures to assess global and local architecture and structural properties of symbol-encoded images are introduced and their usefulness and reliability are discussed in Sec. IV. The results are summarized in Sec. V.

II. DATA

The data, axial slices of 1 mm and 10 mm thickness, were acquired from nonfractured human lumbar vertebrae L3 specimens using a CT scanner Somatom Plus S (Siemens AG) [Fig. 1(a)]. 50 fresh lumbar vertebrae L3 harvested from human cadavers were frozen to $-80\ ^{\circ}\mathrm{C}$ and the vertebral arch was cut off of each vertebra at the level of the spinal canal at the beginning of the pedicels. After thawing, vertebral bodies were examined by high-resolution computed tomography (HRCT) and quantitative computed tomography (QCT) applying an image matrix of 512×512 pixels. HRCT was performed transaxially applying 1 mm slice thickness and an in-plane pixel resolution of 0.182×0.182 mm. Depending on the size of the vertebrae, continuous 28 to 35 slices were obtained. A transaxial center slice of 10 mm thickness, in-plane resolution 0.323×0.323 mm, was obtained and in conjunction with a calibration phantom provided an evaluation of the bone mineral density. The BMD of the specimens ranged from 21 to 122 $\mathrm{mg/cm^3}$. For normal specimens BMD was defined as being above 100 $\mathrm{mg/cm^3}$ (10 specimens), for osteopenic between 80 and 100 $\mathrm{mg/cm^3}$ (14 specimens), and for osteoporotic below 80 $\mathrm{mg/cm^3}$ (26 specimens). 21 specimens were from females (mean age 71 years), 29 from males (mean age 67 years).

III. IMAGE PREPROCESSING

Before the evaluation of structural properties, the region of interest must be separated from the rest of the CT image. Our image preprocessing technique consists of two steps: (i) the vertebral bodies are segmented from the connective and soft tissue background, and then (ii) the entire vertebrae are split into their cortical and cancellous parts. In contrast to standard algorithms [33], which are based on geometrical size of the vertebra and are orientation dependent, we propose orientation and size independent methods based on topological properties (attenuation, edges) of different regions of the CT image.

(i) In order to separate the vertebral body from the rest of the CT image, a soft tissue threshold is specified. There are two main problems in such separation: (a) the attenuation in some regions within the trabecular bone have the same or an even lower value of attenuation as the regions outside the vertebra; (b) the hard cortical outline of the vertebra has holes for blood vessels or low attenuation segments.

Our method is based on a modified algorithm of region growing by pixel aggregation [34]. Instead of one pixel agglomeration as in the simplest case [34], the pixels within the circular ''brush'' are analyzed and agglomerated to the seed area. The idea of this method is as follows: if the diameter brush is set large enough in order to prevent the penetration of the brush into the bone interiors through the gaps in the contour of the filtered vertebra image, the brush pixel aggregation algorithm will remove all the low attenuation pixels outside the vertebra and will preserve all of the vertebra pixels. The procedure is realized by applying a threshold filter at a rather high attenuation level to preserve mainly the cortical shell. The free area (consisting of the connected pixels whose values have been put to zero by the threshold filter) is agglomerated and marked by the brush region growing technique. The resulting largest unmarked area is then the vertebral body, isolated from the other parts of the CT image. This is an effective, fully determined and autonomous algorithm.

(ii) Next, another automatic procedure splits the entire vertebra into two parts: the cancellous bone and the cortical shell. An image of edges is constructed by the application of a one-pixel-edge operator [34]. The edges have a width of one pixel, preserving the image resolution. A draft split is based on the fact that the edges inside the cortical shell are much larger than the edges inside the cancellous bone. This results in a ''draft'' trabecular area. Then, the corrected contour is defined as a closed loop, outside of which the attenuation exceeds a threshold, based on the mean attenuation inside the ''draft'' trabecular area. The region inside this contour is considered as cancellous bone, while the rest of the vertebral body is related to the cortical shell; see Fig. 2.

Cancellous bone has a higher rate of metabolism and this area is affected much faster by metabolic bone diseases. The structural changes of the cancellous bone are evaluated at the next stage of our technique using the concepts of symbolic dynamics and measures of complexity.

IV. SYMBOLIC DYNAMICS FOR TWO-DIMENSIONAL DATA

At this point, the preprocessed CT image is transformed into an image composed of limited types of different sym-

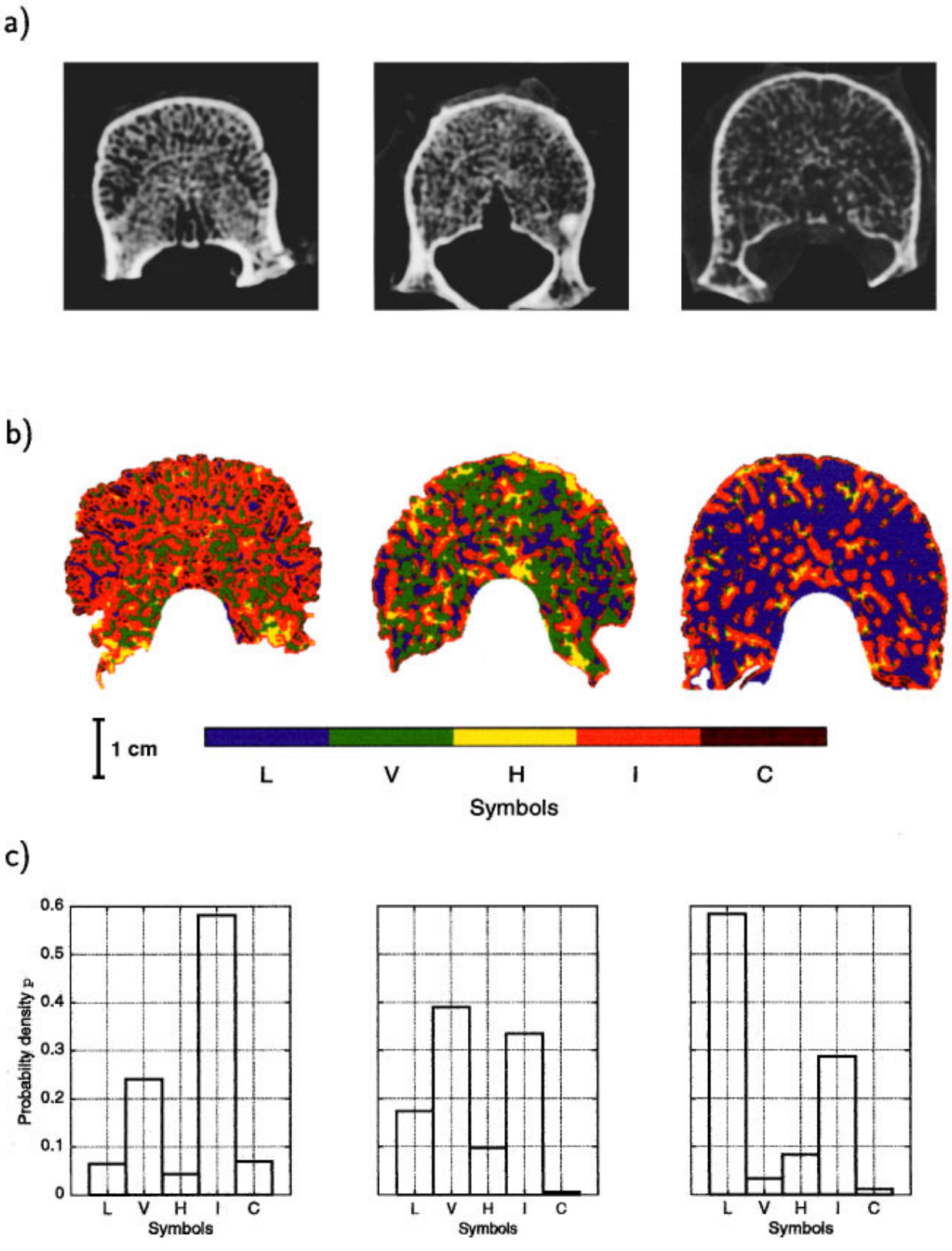

FIG. 1. (Color) Original CT and symbol-encoded images of vertebrae and their corresponding probability density of symbols. (a) Fragments of 1 mm thick axial center CT images of normal (BMD 118 mg/cm^3, left), osteopenic (BMD 81 mg/cm^3, middle), and osteoporotic (BMD 21 mg/cm^3, right) vertebrae. (b) (Color) Corresponding segmented images of cancellous bone transformed into symbols and (c) corresponding probability density of symbols within the cancellous bone.

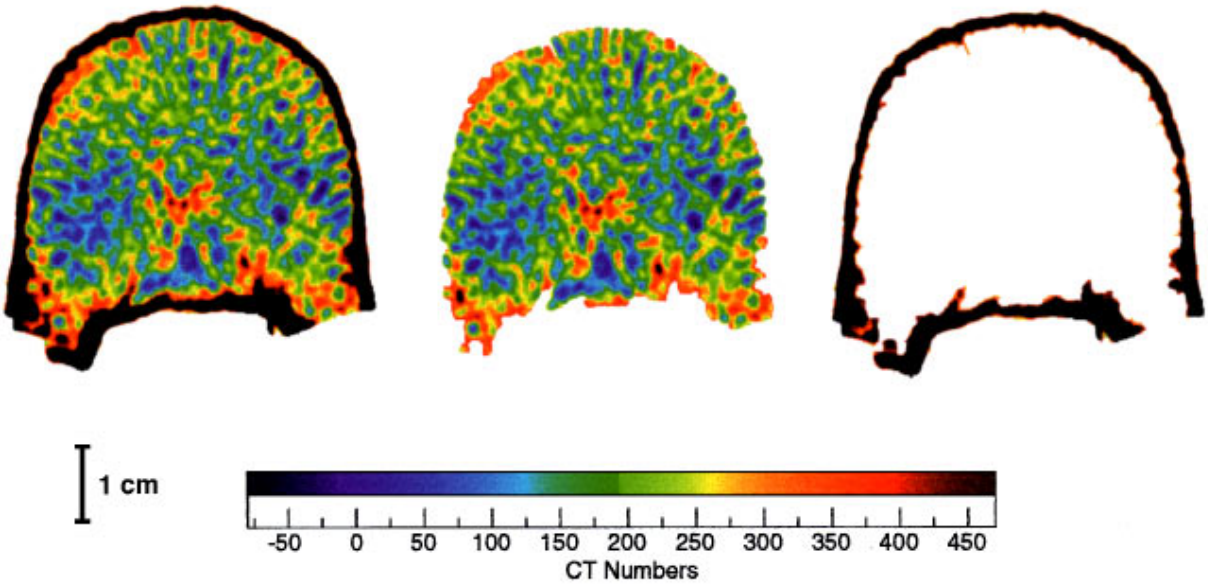

FIG. 2. (Color) Illustration for split procedure: entire vertebra, cancellous bone, and cortical shell (from the axial slice shown in Fig. 1, left).

bols. Instead of representing the image by the large sequence of numbers which sample the x-ray attenuation (4096 gradations are used by our CT scanner), the alternation of symbols is analyzed. While a certain amount of detailed information is lost, but invariant, robust properties of the spatial dynamics and architecture are kept, e.g., regularity, symmetry, global organization of structure, etc. In the best case, such a transformation generates a Markov partition. However, in most examples of natural systems we know neither the existence of such a partition nor their construction. Therefore, more pragmatic transformations have to be used which may not be Markovian ones.

A main point of our method is the introduction of the concept of symbolic dynamics [1,11,35] to analyze two-dimensional objects such as images. Since symbolic dynamics was originally developed to work with multivariate but one-dimensional time series, we have generalized it to the two-dimensional case. The approach consists of two main stages: (i) image encoding and (ii) assessment of the composition of symbols of the encoded image.

A. Image encoding

To perform the transformation into symbols, a set of structural elements or an alphabet of symbols is introduced. From several experiments with different amounts of encoding symbols ranging from 3 to 7, we concluded that 5 is the optimal amount. We use a landscape terminology which is helpful for the understanding of the spatial arrangement of pixel intensities in the images. There are three static elements: L, lake; V, valley; H, highland; combined with two dynamic elements I, incline; C, cliff.

Each pixel of the image at position (x,y) represents the corresponding value of the attenuation $a(x,y)$. For image encoding, two values, mean value of attenuation $\overline{a}$ and standard deviation of attenuation σ_a, and one additional image of edges $e(x,y)$ must be calculated from the pixels representing the object of interest. The map of edges $e(x,y)$ is calculated by the application of a one-pixel-edge operator [34] to the segmented image. Assuming that each pixel at location (x,y) has value a_0 and its eight neighbors have values $a_1,\ldots,a_8$, the one-pixel edge in the given pixel is calculated as

$$e(x,y)=a_0-\min_{i=0,\ldots,8}(a_i). \tag{1}$$

This is a difference of the considered pixel value and a minimal value from nine pixels: the considered pixel by itself and its eight neighbors.

Two encoding parameters must be specified: (a) dynamic-static limit e_{ds} which differentiates static and dynamic encoding; (b) marrow threshold a_m, which separate the pixels representing the bone from the pixels representing the soft marrow tissue. The necessity of fixed specification of the marrow threshold stems from the fact that during osteoporosis a significant part of the bone hard elements are replaced by marrow, but only the hard network is important to keep the shape of the bone. Since the CT scanner is a well-calibrated device, which provides the relationship between CT numbers and the linear x-ray attenuation coefficient, the threshold a_m can be indeed specified.

Finally, each pixel of an object, i.e., $a(x,y)\neq 0$, is encoded by a symbol as follows.

If $e(x,y)<e_{\mathrm{ds}}$, the pixel is coded as a static symbol:

$$L \quad \text{if } a(x,y)\leqslant a_m,$$

$$V \quad \text{if } a_m<a(x,y)\leqslant \overline{a}+\sigma_a,$$

$$H \quad \text{if } a(x,y)>\overline{a}+\sigma_a.$$

If $e(x,y)\geqslant e_{\mathrm{ds}}$, the pixel is coded as a dynamical symbol:

$$I \quad \text{if } e_{\mathrm{ds}}\leqslant e(x,y)\leqslant 3e_{\mathrm{ds}},$$

$$C \quad \text{if } e(x,y)>3e_{\mathrm{ds}}.$$

Several notes about the encoding procedure are important. Our experiments have shown that simple static encoding, also known in image processing as multilevel thresholding [34], is not sufficient to describe the difference of structure in healthy and pathological bones. Therefore, a dynamical refinement of this coding procedure is essential. The dynamical symbols are independent of absolute values of attenuation; they are based on the edge between the current pixel and its neighbors. Yet the encoding algorithm preserves the resolution of the image. Thus a mixture of encoding provides information about both the static and dynamic features of the bone architecture. For example, according to such mixed encoding, an area coded by the symbol L, lake, is an area where not only is the attenuation low, but the spatial dynamics is suppressed as well. Any occurrence of spatial dynamics is encoded by the dynamical symbols I and C independent of the level of the attenuation and such pixels are excluded from the static areas. This is another advantage of the mixed encoding.

Special experiments have shown that the proposed technique is stable for the orientation, density ($21-132$ mg/cm^3) of the bone, and reasonable dispersion of noise influence ($\leqslant 20$ CT numbers). It works at both high- and normal-resolution CT images. Preliminary tests have demonstrated that the technique can be successfully applied to images obtained from patients.

Typical views of encoded normal and pathologic specimens are shown in Fig. 1(b). All three types of structure are clearly distinguished on the symbol-encoded images. Important features of the structure and its spatial dynamics are visualized by such encoding. They are assessed at the next step of our technique.

B. Block of symbols

After encoding, the structural properties of the bone are represented by the composition of symbols within the images. To quantify the spatial arrangement of symbols, its complexity, and local properties of symbol patterns, we introduce the notion ''block of symbols'' of different size. In the one-dimensional case, the signal is transformed into a series of symbols. Typical symbolic patterns within this symbolic string are studied using the notion ''word'': this is just the set of consecutive symbols of a given length [1,11]. For a two-dimensional object, an image, the similar but generalized notion is a block of symbols.

The block of symbols is the connected area composed according to some rules. Two different rules can be used to define the block of symbols.

(i) The block is defined as a square window of size $N\times N$ built around each pixel of the image. The size of the window could vary from 1 to the size of the entire image and symbols of any type can be found within this window. We call such a block *nonempty*, if at least 60% of its pixels belong to the object of interest and are nonvanishing. i.e., $a(x,y)\neq 0$.

(ii) The block is the area composed only by the same symbol or by the same set of symbols which are *connected* to each other. The connection could be considered in a four- or eight-neighborhood system [34]. Using this definition, we can study homogeneous areas formed either from the pixel containing only one chosen type of symbol or a given subset of the used alphabet.

In contrast to a one-dimensional signal analysis, where the sequence of symbols is defined, in image analysis there is no correct way to produce the *sequence* from the two-dimensional *block* of symbols. That is why the arrangement of symbols within the block can only be described either using a statistical approach such as symbol probability density or in terms of pixel connectivity of different groups of symbols.

C. Measures to quantify the structure from symbol-encoded images

In order to assess different aspects of the structure from symbol-encoded images, the probability density of symbols within each block (which is constructed in a different way, see below) must be quantified. The traditional entropy approaches such as that of Shannon [36] or generalized entropy [37] are not appropriate because they solely characterize averaged properties of probability ensembles and are unable to assess the shapes of these distributions with such a small number of bins (five) and dramatic nonsmooth changes of the distribution shape [38] [see Fig. 1(c)].

Several measures M_{XXX} are introduced to quantify different aspects of the structural complexity and composition of the symbol-encoded images.

Three measures are based on the first definition of a block as a square window of size $N\times N$ built around each pixel of the image.

(i) To quantify the complexity of the spatial arrangement of symbols, the structure complexity index (SCI) is introduced. First, from each nonempty block the local distribution of symbols is calculated. Similar distributions of symbols, but obtained from the entire image, are shown in Fig. 1(c). To quantify such a distribution, the well known Shannon entropy [37] is not appropriate, as explained above. Therefore, we propose a measure which we call index of local ensemble (ILE),

$$M_{\mathrm{ILE}}=\frac{p(I)+p(C)}{p(L)+\varepsilon}, \tag{2}$$

where $p(\ )$ is the local probability density of the corresponding symbol and ε is a predefined small value used to avoid division by zero. ILE represents the degree of interstratification of different levels of attenuation and is also the ratio between positive and negative structural elements of the bone. I and C are typical in areas with a developed, rich network of trabeculae. They represent the transition from one level of attenuation to another one and often depict transitions from vertical to horizontal connecting trabeculae. Symbols H and mostly V are found in all stages of pathological structural changes and do not contribute much to the differentiation of those changes by ILE. The symbol L represents the soft marrow tissue located between the hard bone elements.

Next, the analysis of all possible rectangular blocks of the bone image gives the probability density distribution of ILE: p_{ILE}. The Shannon entropy [36] calculated from this distribution as $S(p_{\mathrm{ILE}})=-\Sigma p_{\mathrm{ILE}}\log_2(p_{\mathrm{ILE}})$ is an appropriate mea-

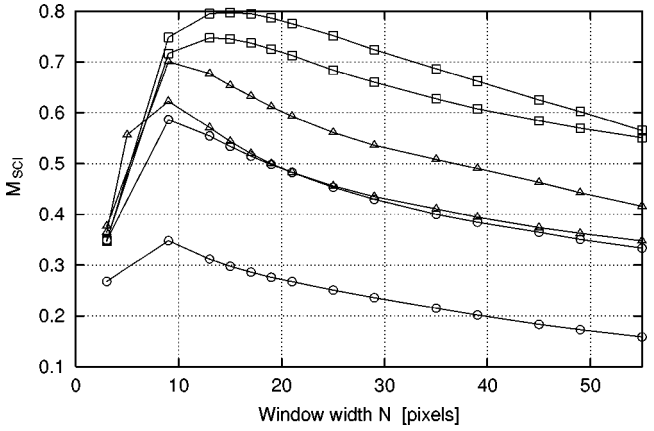

FIG. 3. The dependence of the structure complexity index M_{SCI} on the chosen width of the square window N for two normal (□, upper curves), two osteopenic (△, middle curves), and two osteoporotic cancellous bones (○, lower curves) (from HRCT images).

sure of complexity and characterizes the distribution of local patterns in the bone and is introduced as the structure complexity index (SCI, M_{SCI}). The higher the value of SCI, the more complex and regionally different is the structure, resulting in a more broad, decentralized, and more uniform distribution of local quantities ILE.

Figure 3 shows the dependence of SCI on the window width N for a large range of N. Starting from $N \geqslant 11$, the number of pixels in a local window is large enough for a representative statistical description: at least 121 symbols form the histogram with a domain of five bins. Even in the case of uniform distribution, at least 24 events will be registered in each bin, which provides a rather good statistic. It is important to mention that for $N \geqslant 11$ the window size N does not affect the relation between SCI of normal, osteopenic, and osteoporotic structures. The more N increases, the fewer nonempty windows can be built, and the fewer samples of ILE are calculated. It would result in a poor estimation of the p_{ILE} distribution. In order to obtain enough data to build the distribution of ILE, we chose the window size $N=21$. This is a reasonable compromise between numbers of symbols within one window and numbers of ILE samples (blocks) within the image: 441 symbols are used to construct the five-bin histogram of each window, and the number of blocks per image is usually not less than 1.2×10^4. Depending on the bone size and image resolution, this chosen size of the window is approximately 10–20 % of the trabecular bone width. This is also appropriate from the viewpoint of the characteristic spatial scales of the vertebral architecture.

(ii) To evaluate the orderliness and homogeneity of the trabecular net, the trabecular net index (TNI, M_{TNI}) is introduced. Symbols which represent the trabeculae are V, I, and C (The element H is excluded, since it corresponds sometimes to dense pathologic formations within the cancellous bone, such as osteomas). The distribution of local trabecular quantities $p_{\mathrm{tr}}=p(V)+p(I)+p(C)$ is calculated from small rectangular blocks, similar to the previous measure. Based on this distribution, TNI is defined as

$$M_{\mathrm{TNI}}=\frac{\mathrm{median}(p_{\mathrm{tr}})}{S(p_{\mathrm{tr}})/S_{\max}}. \tag{3}$$

Median and $S(p_{\mathrm{tr}})$ are the median and the Shannon entropy of the p_{tr} distribution, $S(p_{\mathrm{tr}})=-\Sigma p_{\mathrm{tr}}\log_2(p_{\mathrm{tr}})$ and $S_{\max}=\log_2 n$ is the maximal value of the entropy for a given number of bins n in the distribution. In contrast to SCI, $S(p_{\mathrm{tr}})$ characterizes only the organization of hard elements within the architecture.

(iii) To assess the degree of disorder of the cancellous bone structure, from each local block of symbols the following probabilities are calculated: (a) probability of symbol L: $p(L)$, (b) sum of probability of dynamical symbols I and C: $p(I|C)$, (c) sum of probability of two others static symbols V and H: $p(V|H)$. The normalization condition for these probabilities in each block is

$$p(L)+p(I|C)+p(V|H)=1. \tag{4}$$

Next, we construct a three-dimensional space with a system of coordinate axis $p(L)$, $p(I|C)$, $p(V|H)$. Each block of symbols is characterized by the triplet $\{p(L),p(I|C),p(V|H)\}$ and is represented by one point in such 3D probability space. The analysis of all possible nonempty blocks of the image produces a cloud of points in the 3D probability space, and the 3D distribution of the triplets is calculated. The Shannon entropy quantifies the shape of this 3D distribution. The structure disorder index (SDI, M_{SDI}) is the value of the Shannon entropy normalized by the maximal value of the entropy for a given number of bins in the 3D distribution that can be filled by the triplets. Due to the normalization condition (4), only a small area of the 3D probability space can be visited: partition 0.1, 0.1, 0.1 gives only 286 cubic bins fillable by the triplets. Since the number of blocks per image is $\sim10^4$, such a partition of the 3D probability space provides a statistically meaningful description.

The less ordered and less regular the structure is and the larger the difference is in the structural composition in different parts of the bone, the more scattered is the cloud formed by the symbol probability triplets and the larger is the value of the SDI.

(iv) Now we generalize the 1D notion of a word composed only from the given symbol(s). In 2D, this notion is introduced using the second definition of block: a connected area composed only by the same symbol or the same set of symbols. Regions of connected soft tissue within the bone are represented by a connected area encoded by the symbol ''L.'' Their areas are characterized by the size of the L-blocks. An L-block is the connected area composed by pixels encoded by the same symbol ''L.'' The measure $M_{\mathrm{max.}\,L\text{-block}}$ is introduced as the largest size of the L-blocks, normalized by the total bone area.

(v) The last measure we propose assesses the global ensemble of elements (symbols) composing the bone. The distribution of symbols over the entire image is calculated [Fig. 1(c)]. Due to the reasons discussed above, the Shannon entropy is not appropriate to quantify such a distribution. The analog of the ILE [Eq. (2)] but calculated from the entire image instead of small blocks is used: the index of the global ensemble (IGE, M_{IGE}) $M_{\mathrm{IGE}}=[p(I)+p(C)]/[p(L)+\varepsilon]$ is the ratio between probabilities of positive and negative structural elements of the bone.

D. Reproducibility and sensitivity to noise

In order to study the stability of the developed technique against small perturbations of the image, many statistical experiments are performed to check the reliability of the results and to estimate their sensitivity to noise.

First, Gaussian normally distributed white noise of intensity $\sigma_n = 1,2,5$ CT units (which cover the interval 1.5–7 % of mean standard deviation of the signal) is added to the QCT image, and next, the resulting image is quantified by the technique and measures introduced above. It is supposed that different BMD's correspond to different types of the structure. To test how sensitive the proposed measures are to noise for different kinds of structures, eight specimens whose BMD's cover the interval $[20;120]$ mg/cm^3 are taken. For each specimen 50 runs are performed; during each run the underlying structure is slightly perturbed by a different realization of noise. The standard deviation of noise is taken in such a manner that it does not significantly change the type of the underlying structure, but the fine details are smeared. The chosen maximal value of σ_n also corresponds to our estimation of the noise level which is normally present in QCT images. This means that the added white noise doubles the intensity of noise in the image in comparison to the original data. It is important to note that the noise of large intensity simply changes the structure of the image, and this leads to a severalfold shift in values of the structural measures. However, these large intensities of noise are not observed in computed tomography.

The calculations give then 50 samples of each quantity per specimen. They are used to calculate the coefficient of variation $C_V = \sigma_x / \langle x \rangle$. The C_V for different noise intensities and for specimens with different BMD is shown in Fig. 4. We find that the response of symbolic measures on noise perturbation depends on the type of the underlying structure (and on BMD). The results of the evaluation do not differ significantly from one realization of noise to another. The small C_V in the noise experiments indicate that all proposed measures are a robust approach for structural quantification.

Such experiments give us a level to estimate the statistical reliability of the results. The stability of the technique relative to the parameters of the numerical scheme is discussed in Secs. IV A and IV C.

V. RESULTS AND DISCUSSION

The described measures of complexity are applied to the evaluation of bone loss at different stages of osteoporosis. Three groups of specimens have been analyzed: 10 normal, 14 osteopenic, and 26 osteoporotic vertebrae (cf. Sec. II).

The proposed measures of complexity provide a clear qualitative and quantitative distinction between these three kinds of structural organization of bone. Using the results of Sec. IV D, we have checked that this separation between the groups as well as interrelation between BMD and structural complexity is stable against noise. The power of differentiation of all proposed measures is many times greater than their corresponding coefficients of variation (compare Fig. 4 with Fig. 5). Even the maximal L-block size which has the highest C_V also has the largest spread of change. Thus we conclude that all introduced structural quantities provide reliable results.

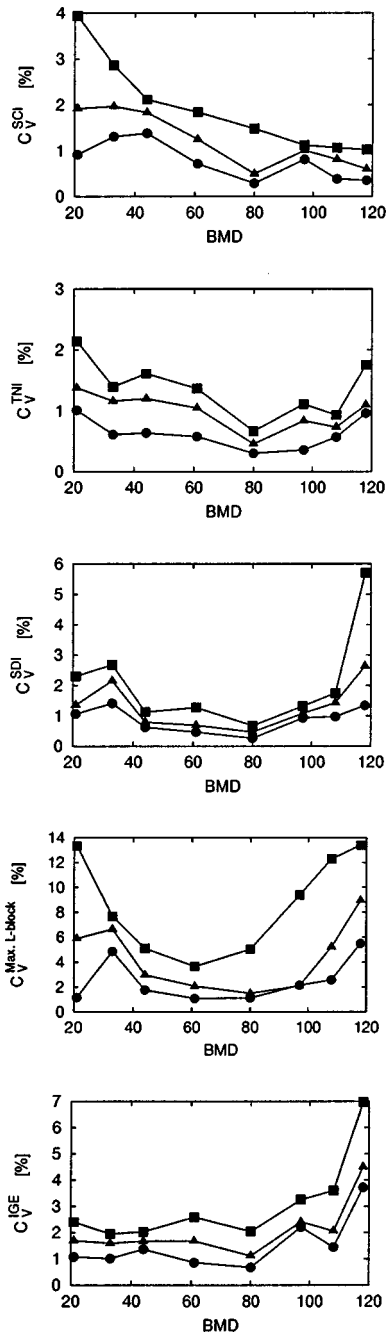

FIG. 4. The coefficient of variation C_V (in %) of different structural measures for specimens with varied bone mineral density (BMD, in mg/cm^3) at different noise levels: (a) structure complexity index (SCI), (b) trabecular net index (TNI), (c) structure disorder index (SDI), (d) size of maximal L-block, and (e) index of global ensemble (IGE). The results are obtained with additional Gaussian white noise of dispersion $\sigma_n = 1,\ 2,$ and 5 CT units being added to the QCT images. Notation of noise intensity: circles, $\sigma_n = 1$; triangles, $\sigma_n = 2$; squares, $\sigma_n = 5$ CT units.

Characteristic types of the cancellous bone architecture and structural changes are detected and quantified by our approach as follows (Fig. 5).

Normal bone. We found that normal bone has a structure with highly developed spatial dynamics. Within the one block (one small square window) normal vertebrae are very inhomogeneous: small areas of low and intermediate attenu-

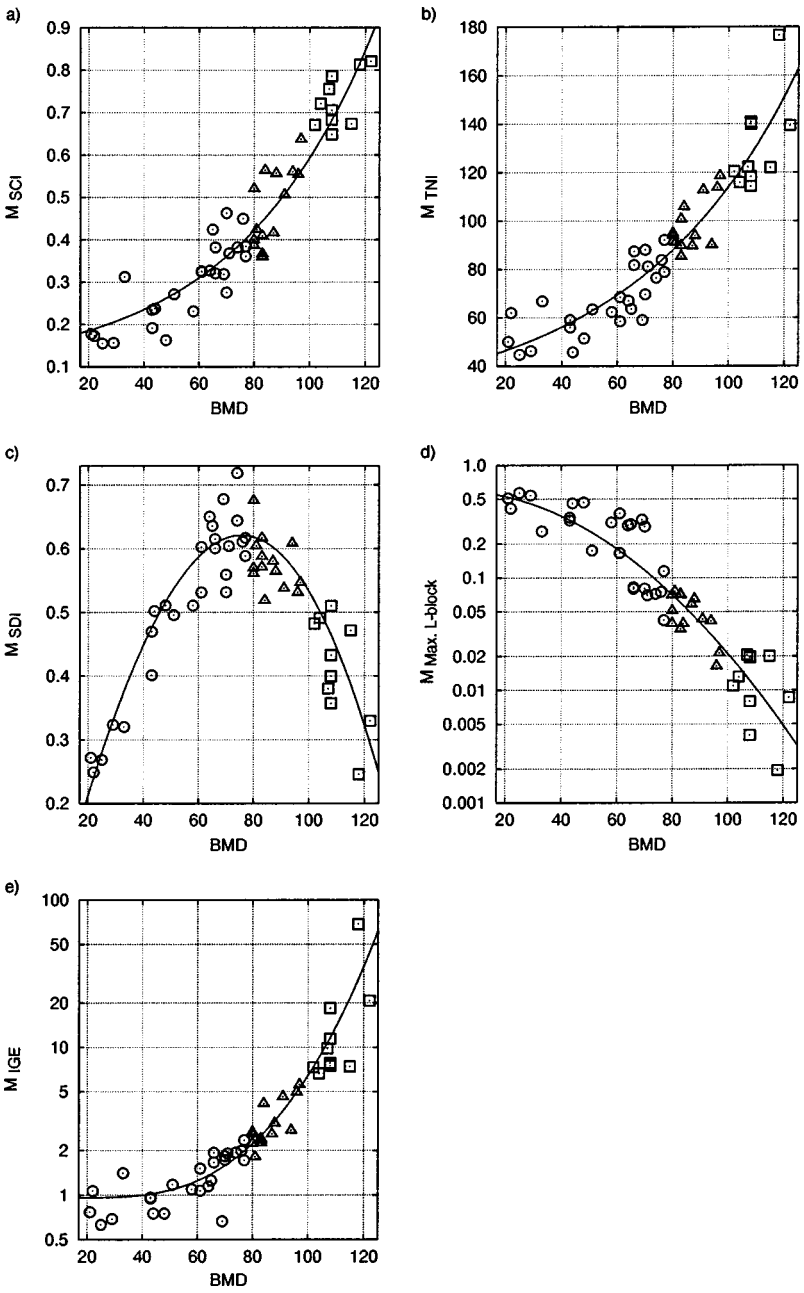

FIG. 5. Diagrams of structural measures of complexity versus bone mineral density (BMD, in mg/cm^3) for different aspects of bone architecture. (a) structure complexity index (SCI), (b) trabecular net index (TNI), (c) structure disorder index (SDI), (d) size of maximal L-block, and (e) index of global ensemble (IGE). A logarithmic scale is used for vertical scales of plots d and e. The results are obtained from the segmented cancellous bone of the 10 mm thick axial center slices. The data in panels a, b, d, e fit an exponential approximation $a_0+a_1\exp^{[a_2+a_3X_{\mathrm{BMD}}]^{a_4}}$ shown by steady curves. The fit in panel (c) has been made by a polynomial of degree 3. The approximation coefficients a_0-a_4 are obtained by the Levenberg-Marquardt algorithm. Notation: □, normal; △, osteopenic; ○, osteoporotic specimens.

ation are intensively interstratified with hard elements and with areas of transition from one level of attenuation to another. The degree of such interstratification, which is represented by the dynamical symbols, differs from the peripheral zone of the cancellous bone to its center and from the front to the back. Nevertheless, it remains at the highest level (Fig. 1). As a result, the SCI has the maximal values for normal cancellous bone [Fig. 5(a)]. The trabecular net has its richest structure, connectivity and complexity: its index TNI is maximal [Fig. 5(b)]. Relatively low values of the SDI show that the structure is rather ordered. The areas of soft tissue (L-blocks) surrounded by hard elements are very small: the size of the largest L-block is less than 2% of the total bone area [Fig. 5(d)]. At the level of the entire cancellous bone composition such type of architecture is represented by the highest probabilities of transitional dynamical symbols I and C, while the element L has a very low probability, which is characterized by the highest values of IGE [Fig. 5(e)]. Measures of complexity, especially SCI, TNI, and SDI demonstrate that a *complex ordered* structure is typical for normal cancellous bone [Figs. 5(a)–5(c)].

Osteopenic bone. Our measures of complexity exhibit that the structure of osteopenic bone significantly differs from normal bone architecture. The differences can be summarized in two simultaneous processes leading to two directions of structural changes in the bone architecture.

(i) The degree of interstratification of attenuation levels is decreased due to the loss of bone. SCI is considerably lower, because the inhomogeneity of the composition within each block is lower. In regions where the trabecular network is still present, the structure as a whole is less complex. The local trabecular quantity p_{tr} is lower, and the entropy of its distribution is higher. It attests that the connectivity of the trabecular net is lower. It is disconnected in many places and its hard elements are replaced by soft tissue. All these facts are captured and summarized by TNI: its value is decreased

significantly by 20 to 40 % (see Fig. 5). Such changes take place approximately in 80% of the cancellous bone area.

(ii) The rest of the bone ($\sim 20\%$) changes completely its architecture. Hard elements almost disappeared and are replaced by soft tissue. These affected spots are represented by the L-blocks. The maximal size of the L-blocks is three to five times larger relative to the normal structure. The occurrence of pronounced affected areas and the increasing disconnection of the trabecular net are quantified by SDI as an increase of disorder within the composition. We conclude that osteopenic bone has *disordered structure with a significantly lower value of complexity* compared to the normal cancellous bone.

Osteoporotic bone. All measures show that the complexity of osteoporotic bone structure is minimal in comparison to normal bone architecture (Fig. 5). Osteoporotic structural patterns are characterized by the lowest IGE. The dominating structural element is L. The spatial dynamics are suppressed and concentrated in separated spots which correspond to columnlike spatial structures (Fig. 1). The value of SCI is three times less than for normal bone structure. The columnlike pattern of the trabecular net leads to the highest entropy of the local trabecular quantity distribution $S(p_{tr})$, the lowest values of p_{tr}, and results in the smallest value of TNI. Abundant uniform soft tissue areas are present. The maximal L-block size increases to 10^2 compared to the normal bone structure. SDI assesses the osteoporotic type of architecture by a low value of disorder. The osteoporotic bone has a *simple ordered structure*.

The behavior of SCI and SDI indicates that during the stages of bone loss there is a transition from one type of bone structure to another—from complex ordered to simple ordered structure—and such a transition happens via an increase of disorder within the architecture. The bell-like parabolic shape of the SDI curve and the monotonous changes of the SCI are in good agreement with the behavior of different measures of complexity, such as fluctuation complexity, the renormalized entropy, and the Renyi entropy, at the transitions in qualitative behavior, as was found for the logistic map [5,39].

The diagrams in Fig. 5 demonstrate the interrelation between two aspects of the bone organization: the amount of available material utilized for its construction (expressed in BMD), as well as the structural characteristics of complexity, disorder, and the quality of the architecture. The results give the first experimental and quantitative evidence of the hypothesis [25,40,41] that the complexity of the bone structure declines rapidly with the increased loss of bone mass. Our study establishes experimentally that the complexity of cancellous bone structure is exponentially related to its density (Fig. 5). The correlation coefficient obtained by using the exponential function and Spearman's nonparametric rank-order correlation coefficient [43] between the bone mineral density and measures quantifying the structure are summarized in Table I. The high correlation indicates a close relationship between measures of bone mass and measures of structural composition. It also confirms the exponential type of interdependence of both properties of bone tissue.

The power of differentiation is much higher than BMD and leads to a significantly higher sensitivity to changes of the bone architecture and integrity. The exponential curves of the proposed measures SCI, TNI, IGE have their steepest slopes in the transitional area between normal and osteopenic vertebrae. This marks the potential of our approach which is highly sensitive to and effective for the detection of initial loss of bone structure and, in addition to the established methods of osteodensitometry [22,23], may help to diagnose metabolic bone diseases early. We suggest that the loss of bone strength and the reduced bone integrity depend on the decreased complexity of the structure.

TABLE I. The correlation coefficient r_{exp} obtained by using the exponential function and Spearman's nonparametric rank-order correlation coefficient r_{rank} between the BMD and the measures of structural complexity.

Measure	r_{exp}	r_{rank}
SCI	0.93	0.95
TNI	0.94	0.96
SDI	0.92[a]	−0.064[b]
Max. L-block	−0.92	−0.94
IGE	0.91	0.96

[a]Using polynomial of degree 3.

[b]Rank-order correlation does not work for a such bell-like dependence.

The complexity of the architecture derives from the contribution of small elements. Complexity measures seize not only parts of bone architecture, but the entirety of the trabecular network, and therefore provide a gauge for the integrity of the bone. However, from a biomechanical standpoint, bone strength is governed by material and structural properties. Bone structure is by definition an adaptive result of bone modeling (bone growth) and remodeling (bone rebuilding) in response to its local stress environment, resulting in the specific sizes and shapes of different bones [42]. A net loss of bone mass leads to an altered stress environment within the bone. Compensatory remodeling and change in architecture is the result as long as this altered architecture and the material properties of the bone tissue can hold the loading stress. A fracture based on osteoporosis is an expression of the decline in bone strength. The structural complexity may explain discrepancies observed in patients with similar low bone densities but different bone frailties. Our findings are also essential criteria to evaluate results from mathematical modeling of the bone. The load-bearing capacity of the architecture is currently being tested on the same specimens with finite element analysis. The results may enable us to determine a correlation between the complexity of the architecture and its capabilities to withstand loading events.

VI. CONCLUSIONS

We generalized the technique of symbolic dynamics to analyze two-dimensional images. The procedure of two-dimensional transformation into symbols is proposed and measures of complexity are utilized to assess the composition of symbols within the images.

This technique is applied to identify structural changes in human cancellous bone of vertebral bodies from preprocessed CT images. Using this technique, we found that the complexity of the structure declines exponentially during the

loss of bone leading to osteoporosis. It is found that normal bone has complex ordered structure, while simple ordered architecture is typical for bones strongly affected by osteoporosis. The transition from normal to osteoporotic architecture happens via an increase of the degree of disorder of the bone composition.

The technique based on symbolic dynamics is more effective than the approaches which use the x-ray attenuation images directly. Complexity measures provide an estimation beyond calculating parameters of architectural fragments, such as the thickness, the number, the space between trabeculae, the volume, or the surface of all elements. Our analysis measures the structure in a holistic way, where the complexity of the structure as a whole is emphasized instead of focusing on the calculation of single parts of the structural composition, while the distribution, the arrangement, and the connectivity of its parts are included as well. The proposed technique is significantly sensitive to change in structure; its idea can be expanded and may well have an impact beyond biological and physical science.

ACKNOWLEDGMENTS

We thank Boehringer Mannheim for support of this research, and the BIOMED Project (Contract No. BMH1–CT92–0296), supported by the EU for the specimens.

[1] B.-L. Hao, Physica D **51**, 161 (1991).
[2] E. Ott, *Chaos in Dynamical Systems* (Cambridge University Press, Cambridge, 1993), p. 108.
[3] P. Grassberger, Int. J. Theor. Phys. **25**, 907 (1986).
[4] J. P. Crutchfield and K. Young, Phys. Rev. Lett. **63**, 105 (1989); in *Complexity, Entropy, and the Physics of Information*, edited by W. Zurek (Addison-Wesley, Reading, MA, 1989), p. 223; J. P. Crutchfield, in *Measures of Complexity and Chaos*, edited by N. Abraham *et al.* (Plenum Press, New York, 1989), p. 327.
[5] R. Wackerbauer, A. Witt, H. Atmanspacher, J. Kurths, and H. Acheingraber, Chaos Solitons Fractals **4**, 133 (1994).
[6] A. Neiman, B. Shulgin, V. Anishchenko, W. Ebeling, L. Schimansky-Geier, and J. Freund, Phys. Rev. Lett. **76**, 4299 (1996).
[7] A. Brandenburg, I. Klapper, and J. Kurths, Phys. Rev. E **52**, 4602 (1995).
[8] U. Schwarz, A. O. Benz, J. Kurths, and A. Witt, Astron. Astrophys. **277**, 215 (1993).
[9] A. Witt, J. Kurths, F. Krause, and K. Fischer, Geophys. Astrophys. Fluid Dyn. **77**, 77 (1995).
[10] A. Witt, A. Neiman, and J. Kurths, Phys. Rev. E **55**, 5050 (1996).
[11] J. Kurths, A. Voss, P. Saparin, A. Witt, H. J. Kleiner, and N. Wessel, Chaos **5**, 88 (1995).
[12] P. E. Rapp *et al.*, Int. J. Bifurcation Chaos Appl. Sci. Eng. **3**, 525 (1993).
[13] P. E. Rapp, A. M. Albano, I. D. Zimmerman, and M. A. Jimenez-Montano, Phys. Lett. A **192**, 27 (1994).
[14] P. I. Saparin, M. A. Zaks, J. Kurths, and V. S. Anishchenko, Phys. Rev. E **54**, 737 (1996).
[15] R. Lakes, Nature (London) **361**, 511 (1993); G. B. Olson, Science **277**, 1237 (1997).
[16] R. Marcus, in *Osteoporosis*, edited by R. Marcus, D. Feldman, and J. Kelsey (Academic Press, San Diego, 1996), p. 647.
[17] S. A. Goldstein, R. Goulet, and D. McCubbrey, Calcif. Tissue Int. **53**, 127 (1993).
[18] Consensus Development Conference [Am. J. Med. **94**, 646 (1993)].
[19] L. J. Melton III, in *Osteoporosis: Etiology, Diagnosis, and Management*, edited by B. L. Riggs and L. J. Melton III (Lippincott-Raven, Philadelphia, 1995), p. 225.
[20] N. F. Fay, J. K. Chan, M. Thamer, and L. J. Melton III, J. Bone Miner. Res. **12**, 24 (1997).
[21] C. Cooper and L. J. Melton III, in *Osteoporosis*, edited by R. Marcus, D. Feldman, and J. Kelsey (Academic Press, San Diego, 1996), p. 419.
[22] H. K. Genant *et al.*, J. Bone Miner. Res. **11**, 707 (1996); L. Lenchik and D. J. Sartoris, AJR, Am. J. Roentgenol. **168**, 905 (1997); *Bone Densitometry and Osteoporosis*, edited by H. K. Genant, G, Gugliemi, and M. Jergas (Springer-Verlag, Berlin, 1998).
[23] D. Felsenberg, in *Metabolische Osteopathien*, edited by M. J. Siebel and H. Stracke (Schattauer Verlag, Stuttgart, 1997), p. 65.
[24] L. A. Feldkamp, S. A. Goldstein, A. M. Parfitt, G. Jesion, and M. Kleerekoper, J. Bone Miner. Res. **4**, 3 (1989).
[25] T. J. Beck, Radiology **199**, 612 (1996).
[26] A. M. Parfitt, C. H. E. Mathews, A. R. Villanueva, and M. Kleerekoper, J. Clin. Invest. **72**, 1396 (1983).
[27] M. Kleerekoper, A. R. Villanueva, J. Stanciu, D. Sudhaker Rao, and A. M. Parfitt, Calcif. Tissue Int. **37**, 594 (1985); A. Vesterby, H. J. G. Gundersen, and F. Melsen, Bone (N.Y.) **10**, 7 (1989); R. S. Weinstein and M. S. Hutson, *ibid.* **8**, 137 (1987).
[28] R. Rüegsegger, B. Koller, and R. Müller, Calcif. Tissue Int. **58**, 24 (1996).
[29] S. Majumdar, R. S. Weinstein, R. R. Prased, and H. K. Genant, Calcif. Tissue Int. **52**, 168 (1993); J. C. Buckland-Wright, J. A. Lynch, J. Rymer, and I. Fogelman, *ibid.* **54**, 106 (1994).
[30] M. Ito *et al.*, Radiology **194**, 55 (1995).
[31] R. Klepper, C. Johner, and R. D. Hesch, RöFo, Fortsch. Röntgenst. **159**, 337 (1993).
[32] C. L. Gordon, C. E. Webber, J. D. Adachi, and N. Christoforou, Phys. Med. Biol. **41**, 495 (1996).
[33] W. A. Kalender, W. Bautz, and D. Felsenberg, Digit. Bilddiagn. **7**, 66 (1987); E. Klotz, W. A. Kalender, and T. Sandor, IEEE Trans. Med. Imaging **8**, 371 (1989).
[34] R. Klette and P. Zamperoni, *Handbook of Image Processing Operators* (John Wiley & Sons, Chichester, UK, 1996); R. C. Gonzalez and R. E. Woods, *Digital Image Processing* (Addison-Wesley, Reading, MA, 1992).
[35] F. Spahn, U. Schwarz, and J. Kurths, Phys. Rev. Lett. **78**, 1596 (1997).
[36] C. E. Shannon and W. Weaver, *The Mathematical Theory of*

Communication (University of Illinois Press, Urbana, 1949).
[37] J. Balatoni and A. Renyi, in *Selected Papers of A. Renyi* (Academiau, Budapest, 1976), Vol. 1, p. 558.
[38] P. Saparin, W. Gowin, J. Kurths, and D. Felsenberg, AIP Conf. Proc. **411**, 347 (1997).
[39] P. Saparin, A. Witt, J. Kurths, and V. Anishchenko, Chaos Solitons Fractals **4**, 1907 (1994).
[40] M. J. Silva and L. J. Gibson, Bone (N.Y.) **21**, 191 (1997).
[41] T. A. Einhorn, in *Osteoporosis*, edited by R. Marcus, D. Feldman, and J. Kelsey (Academic Press, San Diego, 1996), p. 3.
[42] J. Wolff, Arch. Path. Anat. Phys. **155**, 256 (1899).
[43] W. H. Press, S. A. Teukolsky, W. T. Vetterling, and A. B. Flannery, *Numerical Recipes in C: The Art of Scientific Computing* (Cambridge University Press, Cambridge, 1995).